Human-Induced Changes in the Hydrology of the Western United States

Tim P. Barnett,[1]* David W. Pierce,[1] Hugo G. Hidalgo,[1] Celine Bonfils,[2] Benjamin D. Santer,[2] Tapash Das,[1] Govindasamy Bala,[2] Andrew W. Wood,[3] Toru Nozawa,[4] Arthur A. Mirin,[2] Daniel R. Cayan,[1,5] Michael D. Dettinger[1,5]

Observations have shown that the hydrological cycle of the western United States changed significantly over the last half of the 20th century. We present a regional, multivariable climate change detection and attribution study, using a high-resolution hydrologic model forced by global climate models, focusing on the changes that have already affected this primarily arid region with a large and growing population. The results show that up to 60% of the climate-related trends of river flow, winter air temperature, and snow pack between 1950 and 1999 are human-induced. These results are robust to perturbation of study variates and methods. They portend, in conjunction with previous work, a coming crisis in water supply for the western United States.

Water is perhaps the most precious natural commodity in the western United States. Numerous studies indicate the hydrology of this region is changing in ways that will have a negative impact on the region (1–3). Between 1950 and 1999 there was a shift in the character of mountain precipitation, with more winter precipitation falling as rain instead of snow (2, 4, 5), earlier snow melt (4, 6), and associated changes in river flow (7–10). In the latter case, the river flow experiences relative increases in the spring and relative decreases in the summer months. These effects go along with a warming over most of the region that has exacerbated these drier summer conditions (5, 8, 11).

The west naturally undergoes multidecadal fluctuations between wet and dry periods (12). If drying from natural climate variability is the cause of the current changes, a subsequent wet period will likely restore the hydrological cycle to its former state. But global and regional climate models forced by anthropogenic pollutants suggest that human influences could have caused the shifts in hydrology (2, 13–15). If so, these changes are highly likely to accelerate, making modifications to the water infrastructure of the western United States a virtual necessity.

Here, we demonstrate statistically that the majority of the observed low-frequency changes in the hydrological cycle (river flow, temperature, and snow pack) over the western United States from 1950 to 1999 are due to human-caused climate changes from greenhouse gases and aerosols. This result is obtained by evaluating a combination of global climate and regional hydrologic models, together with sophisticated data analysis. We use a multivariable detection and attribution (D&A) methodology (16–18) to show that the simultaneous hydroclimatic changes observed already differ significantly in length and strength from trends expected as a result of natural variability (detection) and differ in the specific ways expected of human-induced effects (attribution). Focusing on the hydrological cycle allows us to assess the origins of the most relevant climate change impacts in this water-limited region.

We investigated simultaneous changes from 1950 to 1999 (19) in snow pack (snow water equivalent or SWE), the timing of runoff of the major western rivers, and average January through March daily minimum temperature (JFM T_{min}) in the mountainous regions of the western United States (20). These three variates arguably are among the most important metrics of the western hydrological cycle. By using the multivariable approach, we obtain a greater signal-to-noise (S/N) ratio than from univariate D&A alone (see below).

The SWE data are normalized by October-to-March precipitation (P) to reduce variability from heavy- or light-precipitation years. Observed SWE/P and temperature were averaged over each of nine western mountainous regions (Fig. 1) to reduce small-spatial-scale weather noise. The river flow variate is the center of timing (CT), the day of the year on which one-half of the total water flow for the year has occurred, computed from naturalized flow in the Columbia, Colorado, and Sacramento/San Joaquin rivers. CT tends to decrease with warming because of earlier spring melting.

Selected observations from these regions and variables are displayed in Fig. 2, showing the trends noted above, along with substantial regional differences and "weather noise." SWE/P trends in the nine regions vary from –2.4 to –7.9% per decade, except in the southern Sierra Nevada where the trend is slightly positive. The JFM T_{min} trends are all positive and range from 0.28° to 0.43°C per decade, whereas the river CT
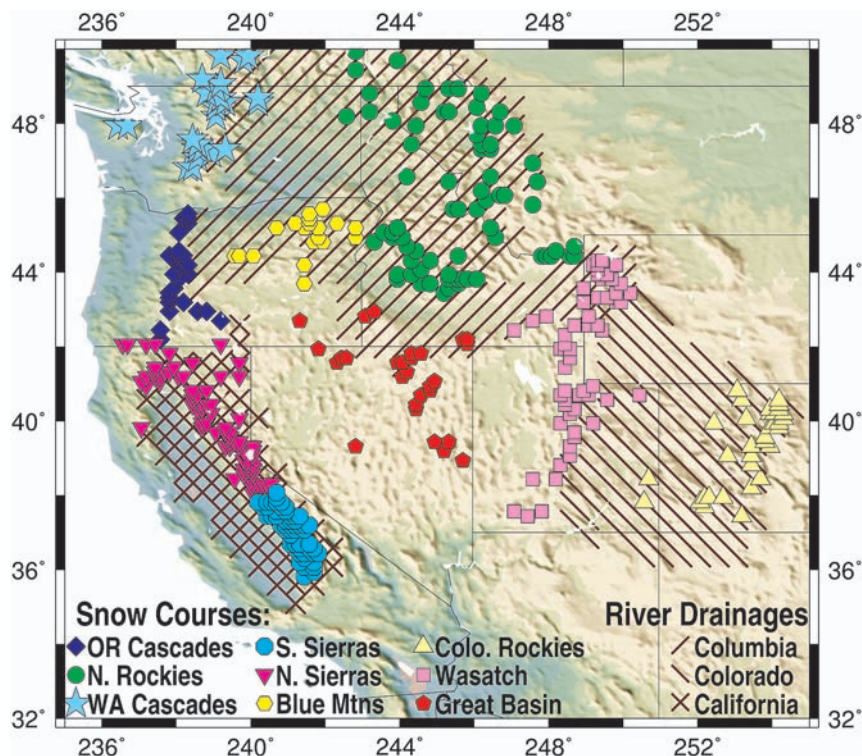
[1]Scripps Institution of Oceanography, University of California, San Diego, La Jolla, CA 92093, USA. [2]Lawrence Livermore National Laboratory, Livermore, CA 94550, USA. [3]Land Surface Hydrology Research Group, Civil and Environmental Engineering, University of Washington, Seattle, WA 98195, USA. [4]National Institute for Environmental Studies, 16-2, Onogawa, Tsukuba, Ibaraki 305-8506, Japan. [5]U.S. Geological Survey, La Jolla, CA 92093, USA.

*To whom correspondence should be addressed. E-mail: tbarnett-ul@ucsd.edu

Fig. 1. Map showing averaging regions over which SWE/P and JFM T_{min} were determined. The hatching shows the approximate outline of the three main drainage basins used in this study.

arrives from 0.3 to 1.7 days per decade earlier. The challenge in D&A analysis is to determine whether a specific, predetermined signal representing the response to external forcing is present in these observations.

We compared the observations with results from a regional hydrologic model forced by global climate model runs. One of the global models, the Parallel Climate Model (PCM) (*21*), has been used previously in hydrological studies in the western United States (*22*) and realistically portrays important features of observed climate and the amplitude of natural internal variability. The second climate model, the anthropogenically forced medium-resolution Model for Interdisciplinary Research on Climate (MIROC) (*23–25*), was selected from the current Intergovernmental Panel on Climate Change (IPCC) AR4 set of global runs (*26*) because it had available many

20th-century ensemble members with daily data, and because it offered a high degree of realism in representing the Pacific Decadal Oscillation (PDO). We used the anthropogenically forced versions of these models to obtain an estimate for the expected signal not confounded by other forcing mechanisms. The models provided multiple realizations (10 for MIROC, 4 for PCM) of the historical response of the climate system to anthropogenic forcing. The daily output from these coarse-horizontal-resolution model results was downscaled to a 1/8° × 1/8° latitude-longitude grid by two different statistical methods [Bias Correction and Spatial Disaggregation (BCSD) (*27*) and Constructed Analogues (CA) (*28*)]. The downscaled temperature and precipitation data were supplied as input to the Variable Infiltration Capacity (VIC) hydrological model (*15, 27, 29*) to obtain river flow and SWE/P.

We used the downscaled model results to estimate an anthropogenic "fingerprint" for the PCM and MIROC models (*30*). The fingerprint describes the joint variability of SWE/P, JFM T_{min}, and river flow (Fig. 3) (*20*). The model fingerprints are very similar despite the different external forcings used (*20, 26*). The results show that warmer temperatures accompany decreases in SWE/P and decreases in CT of major western river systems. The sign of each variable is a monopole, indicating a coherent regional-scale signal over the western United States.

The temporal component of the fingerprint (not shown) is well represented by a simple trend. This implies that the fingerprint primarily captures the spatial expression of long-term changes, and not shorter-period climate modes (such as El Niño–Southern Oscillation or the PDO).

The signal strength is calculated as the least-squares linear trend of the projection of a data set (model or observations) onto the fingerprint (*20*). The upper panel of Fig. 4 shows the ensemble mean signals for our various model runs and the observations (*20*). The observations show a positive signal indistinguishable from the PCM and MIROC anthropogenically forced runs. These signals exclude zero at the 95% confidence interval, thus achieving "detection."

We used 1600 years of downscaled control run data from two different global models (*20*) to estimate the probability that the observed signal could be due to natural, internal variability (Fig. 4, lower panel). The observed signal falls outside the range expected from natural variability with high confidence ($P < 0.01$). In separate analyses for PCM and MIROC, the likelihood that the model signal arises from natural internal variability is between 0.01 and 0.001 (*20*). The different downscaling methods have little impact on these results. We conclude that natural internal climate variability alone cannot explain either the observed or simulated changes in SWE/P, JFM T_{min}, and CT in response to anthropogenic forcing.

PCM simulations forced solely by the combined impacts of observed solar variability and volcanic activity (Sol/Vol, Fig. 4) show a signal with sign opposite to that observed. We conclude that solar and volcanic forcing also fail to explain the observed hydrological changes.

Might anthropogenically induced precipitation changes account for our results? This is unlikely because our variables were chosen to minimize sensitivity to precipitation fluctuations. However, previous work has identified an anthropogenic effect on global-scale changes in precipitation (*31*). We conducted a univariate D&A analysis on precipitation, comparing the fingerprint obtained from the anthropogenic runs to the control runs and observations. The results (Fig. 4, lower panel) show that the observed changes in precipitation over the nine western U.S. mountain regions are indistinguishable from natural variability. We found the same for model precipitation (not shown). We conclude that although
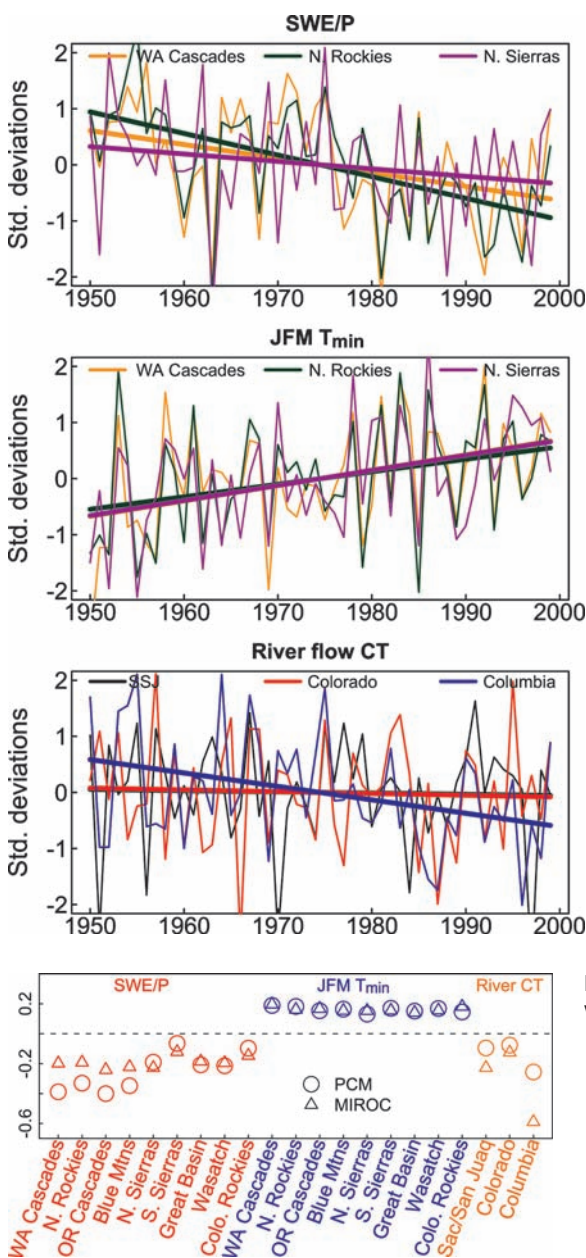

Fig. 2. Observed time series of selected variables (expressed as unit normal deviates) used in the multivariate detection and attribution analysis. Taken in isolation, seven of nine SWE/P, seven of nine JFM T_{min}, and one of the three river flow variables have statistically significant trends.

Fig. 3. Fingerprints from the multivariate analysis of PCM and MIROC.

precipitation may be affected by anthropogenic forcing on larger scales or in other regions, or in this region in the future, it cannot explain the strong changes in western U.S. hydrology from 1950 to 1999.

Finally, the observations are consistent with the anthropogenic model runs. The observed signal is stronger than found in either model, but
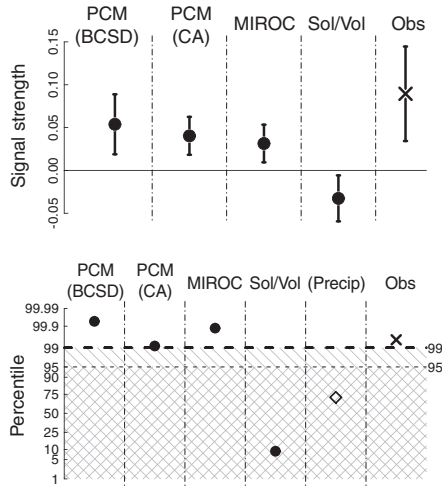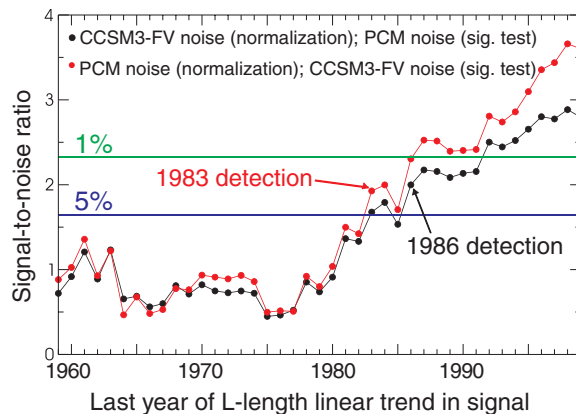

Fig. 4. Ensemble average signal strength (upper panel; standard deviations of the fingerprint's principal component per decade) and percentile rank of ensemble mean signal strength for the indicated model runs with respect to the combined (CCSM3-FV and PCM) control run (lower panel). Percentile values were calculated by Monte Carlo resampling of the control run taking into account N, the varying number of ensemble members. PCM (BCSD) and PCM (CA): PCM runs with anthropogenic forcing, with two different downscaling methods as described in the text ($N = 4$). MIROC: MIROC runs with anthropogenic forcing ($N = 10$). Sol/Vol: PCM runs with only solar and volcanic forcing included ($N = 2$). The cross shows the signal strength obtained from the observations ($N = 1$). For comparison purposes, also shown is the observed signal strength from a separate analysis of precipitation changes over the nine mountain regions (diamond). Values outside the hatched and cross-hatched regions are significant at the 0.01 and 0.05 levels, respectively.

Fig. 5. Time-dependent S/N estimates for two different estimates of natural variability. The x axis is the last year of L-length linear trend in the signal estimate.

the differences are not statistically significant. The ensemble mean signal strength from PCM is 60% of the observed signal strength; that is, PCM estimates that three-fifths of the projected trend can be ascribed to human effects. The two downscaling methods give somewhat different signal strengths (Fig. 4), but the attribution holds no matter which is chosen. We conclude that application of a rigorous, multivariable D&A methodology shows a detectable and attributable signature of human effects on western hydrology.

We examined the time evolution of signal and noise by projecting the observations (signal) and control run data (noise) onto the multivariable fingerprint, then fitting linear trends of increasing length L to the resulting projected time series. This enabled us to calculate a S/N ratio as a function of L (from 10 to 50 years); Fig. 5 shows that the S/N ratio rises above the 5% significance threshold no later than 1986. This result is robust to uncertainties in the model fingerprint, model-based noise estimates, and statistical downscaling method (20). We also repeated the D&A analysis without areal weighting and found that it made no difference in our conclusions.

The variables examined here covary in a physically and internally consistent way: An increase in minimum temperature is associated with less SWE/P and earlier runoff. Quantitatively, we also compared the S/N obtained from separate analyses of each variable with that obtained for the full multivariable problem (20). For fixed choices of fingerprint, noise, and downscaling (32), the S/N values from the separate SWE/P, JFM T_{min}, and CT analyses were 2.90, 2.95, and 1.85, respectively, all significant at about the 0.05 level or above. The multivariable analysis had a S/N of 3.62, and so it has quantitative value as well as providing a test of whether SWE/P, JFM T_{min}, and CT covary in a physically consistent way.

Our results are robust with respect to uncertainties in model estimates of anthropogenic climate fingerprints and natural variability, downscaling method, and the choice of univariate or multivariate D&A analysis. Estimates of natural variability used for significance testing agree well with those derived from paleo proxies (20). The analyses show with high confidence that

the majority of the detrimental changes already seen in western U.S. hydrology are caused by human-induced effects. PCM, which has the most realistic signal strength, shows that human effects account for 60% of the observed 1950–1999 trend in signal strength. MIROC accounts for 35% of the trend. On the basis of Fig. 4 (upper panel) and the discussion of MIROC in (20), the PCM number seems more reliable.

Our results are not good news for those living in the western United States. The scenario for how western hydrology will continue to change has already been published using one of the models used here [PCM (2)] as well as in other recent studies of western U.S. hydrology [e.g., (15)]. It foretells water shortages, lack of storage capability to meet seasonally changing river flow, transfers of water from agriculture to urban uses, and other critical impacts. Because PCM performs so well in replicating the complex signals of the last half of the 20th century, we have every reason to believe its projections and to act on them in the immediate future.

References and Notes
1. P. Gleick, *Water Resour. Res.* **23**, 1049 (1987).
2. ACPI, The Accelerated Climate Prediction Initiative, *Clim. Change* **62**, 444 (2004).
3. B. Udall, G. Bates, *Intermountain West Climate Summary, Western Water Assessment*, January 2007 (available from University of Colorado).
4. A. F. Hamlet, P. W. Mote, M. P. Clark, D. P. Lettenmaier, *J. Clim.* **18**, 4545 (2005).
5. N. Knowles, M. D. Dettinger, D. R. Cayan, *J. Clim.* **19**, 4545 (2006).
6. P. W. Mote, A. F. Hamlet, M. P. Clark, D. P. Lettenmaier, *Bull. Am. Meteorol. Soc.* **86**, 39 (2005).
7. M. D. Dettinger, D. R. Cayan, *J. Clim.* **8**, 606 (1995).
8. D. R. Cayan, S. Kammerdiener, M. D. Dettinger, J. Caprio, D. Peterson, *Bull. Am. Meteorol. Soc.* **82**, 399 (2001).
9. I. T. Stewart, D. R. Cayan, M. D. Dettinger, *J. Clim.* **18**, 1136 (2005).
10. S. K. Regonda, B. Rajagopalan, M. Clark, J. Pitlick, *J. Clim.* **18**, 372 (2005).
11. P. Y. Groisman et al., *J. Hydrometeorol.* **5**, 64 (2003).
12. Colorado River Basin Water Management, *Evaluating and Adjusting to Hydroclimatic Variability* (National Academy of Sciences, Washington, DC, 2007).
13. P. C. D. Milly, K. A. Dunne, A. V. Vecchia, *Nature* **438**, 347 (2005).
14. R. Seager et al., *Science* **316**, 1181 (2007); published online 4 April 2007 (10.1126/science.1139601).
15. N. Christiansen, D. Lettenmaier, *Hydrol. Earth Syst. Sci. Discuss.* **3**, 1 (2006).
16. T. P. Barnett, M. Schlesinger, *J. Geophys. Res.* **92**, 14772 (1987).
17. B. D. Santer et al., *Clim. Dyn.* **12**, 77 (1995).
18. R. Schnur, K. I. Hasselmann, *Clim. Dyn.* **24**, 45 (2005).
19. Note that this period excludes the large-scale changes in runoff, precipitation, and water storage that have occurred in the southwest, especially the Colorado River drainage, since 2000. We do not claim that the large changes since 2000 are necessarily the result of human-induced warming.
20. See supporting material on *Science* Online.
21. W. Washington et al., *Clim. Dyn.* **16**, 755 (2000).
22. T. P. Barnett et al., *Clim. Change* **62**, 1 (2004).
23. K-1 Model Developers, *K-1 Coupled Model (MIROC) Description (K-1 Technical Report 1)*, H. Hasumi, S. Emori, Eds. (Center for Climate System Research, University of Tokyo, 2004).
24. T. Nozawa et al., *Geophys. Res. Lett.* **32**, L20719 (2005).
25. T. Nozawa et al., *MIROC, CGER's Supercomputer Monograph Report 12* (Center for Global Environmental Research, National Institute for Environmental Studies, Tsukuba, Japan, 2007).

26. B. D. Santer *et al.*, *Proc. Natl. Acad. Sci. U.S.A.* **104**, 15248 (2007).
27. A. Wood *et al.*, *Clim. Dyn.* **16**, 755 (2004).
28. E. P. Maurer, H. G. Hidalgo, *Hydrol. Earth Syst. Sci. Discuss.* **4**, 3413 (2007).
29. X. Liang, D. Lettermaier, A. Wood, S. Burges, *J. Geophys. Res.* **99**, 14415 (1994).
30. T. P. Barnett *et al.*, *Science* **309**, 284 (2005); published online 2 June 2005 (10.1126/science.1112418).
31. X. Zhang *et al.*, *Nature* **448**, 461 (2007).
32. The choices were CCSM3-FV noise for significance testing, PCM fingerprint, and statistical downscaling with the CA method. In the multivariable case, PCM noise was used for normalization.
33. The MIROC data were generously supplied by the National Institute for Environmental Studies, Onogawa, Tsukuba, Ibaraki, Japan. The PCM simulation had previously been made available to the Scripps Institution of Oceanography (SIO) by the National Center for Atmospheric Research for the Accelerated Climate Prediction Initiative project. Supported by the Lawrence Livermore National Laboratory (LLNL) through a Laboratory-Directed Research and Development grant to SIO via the San Diego Super Computer Center for the LUCSiD project; the U.S. Department of Energy and NOAA through the International Detection and Attribution Group (T.P.B.); Program of Climate Model Diagnoses and Intercomparison grant DOE-W-7405-ENG-48 (C.B., B.D.S., G.B., A.A.M.); the U.S. Geological Survey and SIO (D.R.C., M.D.D.); and the California Energy Commission (D.W.P., H.G.H.).

Atomic-Level Models of the Bacterial Carboxysome Shell

Shiho Tanaka,[1] Cheryl A. Kerfeld,[3,4] Michael R. Sawaya,[2] Fei Cai,[5] Sabine Heinhorst,[5] Gordon C. Cannon,[5] Todd O. Yeates[1,2]*

The carboxysome is a bacterial microcompartment that functions as a simple organelle by sequestering enzymes involved in carbon fixation. The carboxysome shell is roughly 800 to 1400 angstroms in diameter and is assembled from several thousand protein subunits. Previous studies have revealed the three-dimensional structures of hexameric carboxysome shell proteins, which self-assemble into molecular layers that most likely constitute the facets of the polyhedral shell. Here, we report the three-dimensional structures of two proteins of previously unknown function, CcmL and OrfA (or CsoS4A), from the two known classes of carboxysomes, at resolutions of 2.4 and 2.15 angstroms. Both proteins assemble to form pentameric structures whose size and shape are compatible with formation of vertices in an icosahedral shell. Combining these pentamers with the hexamers previously elucidated gives two plausible, preliminary atomic models for the carboxysome shell.

The carboxysome enhances CO_2 fixation inside many photosynthetic and chemoautotrophic bacterial cells by encapsulating the key enzymes ribulose-1,5-bisphosphate carboxylase-oxygenase (RuBisCO) and carbonic anhydrase (*1–3*). In contrast to membrane-bound eukaryotic organelles, carboxysomes and related bacterial microcompartments (*4, 5*) have a proteinaceous outer shell, which is roughly polyhedral in shape (Fig. 1). The earliest observations of carboxysomes by electron microscopy date back more than 40 years (*6, 7*). Subsequent genetic and biochemical studies have provided essential information about their function and composition (*3, 8–10*); structural studies (*11–14*) have begun to illuminate the functional mechanisms and architectural details of the carboxysome.

Carboxysomes are found in all cyanobacteria and in some chemoautotrophic bacteria. Two types of carboxysomes have been defined by patterns of genomic organization and by protein sequence comparisons (*15*). They are represented in two model organisms, *Halothiobacillus neapolitanus*

[1]Department of Chemistry and Biochemistry, University of California at Los Angeles (UCLA), Los Angeles, CA 90095, USA. [2]UCLA–Department of Energy Institute for Genomics and Proteomics, Los Angeles, CA 90095, USA. [3]Department of Energy–Joint Genome Institute, Walnut Creek, CA 94598, USA. [4]Department of Plant and Microbial Biology, University of California, Berkeley, CA 94720, USA. [5]Department of Chemistry and Biochemistry, University of Southern Mississippi, Hattiesburg, MS 39406, USA.

*To whom correspondence should be addressed. E-mail: yeates@mbi.ucla.edu
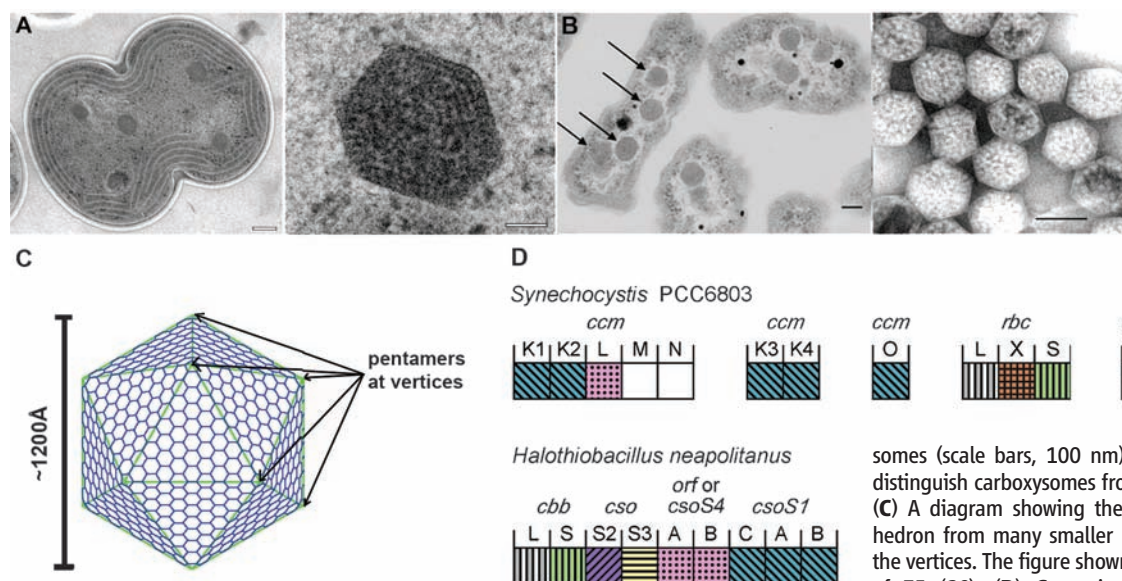
Fig. 1. Carboxysome architecture and operon organization. Transmission electron micrographs showing (**A**) (left) a section through a dividing cyanobacterial cell, *Syn.* 6803 (scale bar, 200 nm), and (right) an enlargement of a single carboxysome (scale bar, 50 nm) and (**B**) (left) *Halothiobacillus neapolitanus* cells with their carboxysomes highlighted by arrows and (right) purified carboxysomes (scale bars, 100 nm). Their polyhedral shape helps distinguish carboxysomes from other cytoplasmic inclusions. (**C**) A diagram showing the construction of a large icosahedron from many smaller hexagons and 12 pentagons at the vertices. The figure shown has a triangulation number (T) of 75 (*29*). (**D**) Genomic arrangement of carboxysome-associated proteins. Homologous proteins from the two model organisms are shaded and colored similarly. The hexameric shell proteins are colored in blue. The CcmL and OrfA (or CsoS4A) proteins under study here are colored in pink. The *rbc* and *cbb* genes code for the large and small subunit of RuBisCO. (A) is adapted from ref. (*11*); (B) is adapted from ref. (*12*).